

Effects of oscillating spacetime metric background on a complex scalar field and formation of topological vortices

Shreyansh S. Dave^{1,*} and Sanatan Dikal^{1,2,†}

¹*The Institute of Mathematical Sciences, Chennai 600113, India*

²*Homi Bhabha National Institute, Training School Complex, Anushakti Nagar, Mumbai 400085, India*

We study the time evolution of a complex scalar field in the symmetry broken phase in the presence of oscillating spacetime metric background. In our (2+1)-dimensional simulations, we show that the spacetime oscillations can excite an initial field configuration, which ultimately leads to the formation of topological vortices in the system. At late times, field configuration achieves a *disordered state*. A detailed study of the momentum and frequency modes of the field reveals that these field excitations are driven by the phenomena of *parametric resonance*. At extremely high frequency regime where frequency of spacetime oscillations is much larger than the field-mass, the formed vortices are not topological in nature. Interestingly in this regime, for a suitable choice of parameters of the simulation, we observe a persistent lattice structure of vortex-antivortex pairs. We discuss applications of our study to the dynamics of interior superfluidity of neutron stars during the binary neutron star mergers, in generation of excitation of ultralight axion-like field near a strong gravitational wave source, etc.

I. INTRODUCTION

Topological defects arise in systems ranging from condensed matter to the early Universe [1, 2]. They exist in systems which have topologically non-trivial order parameter space (or vacuum manifold). There are many condensed matter systems, such as superfluid, superconductor, nematic liquid crystal etc., which have topologically non-trivial order parameter space in their respective symmetry broken phases, therefore allow the existence of topological defects. For example, the superfluid phase of ⁴He is characterized by a complex wavefunction. The corresponding order parameter space is a circle S^1 , for which the *fundamental group* is non-trivial, i.e. $\pi_1(S^1)=\mathbb{Z}$ [3]. Therefore this system allows the existence of topological vortices. The vortices are characterised by different elements of the fundamental group.

There are various ways by which topological defects can form in a physical system. These defects produce during a spontaneous symmetry breaking phase transition, which can be described by the *Kibble mechanism* [4]. There are other methods also by which topological defects can be nucleated in a system. For example, in superfluid ⁴He, the rotation of vessel within a range of angular velocity leads to the generation of vortex lattice [5, 6]. Similarly, in the type-II superconductor, an external magnetic field within a range of field strength leads to the formation of flux-tube lattice [5, 6].

In refs.[7, 8], the formation of defect-antidefect pairs has been studied in Φ^4 theories with time dependent temperature in the effective potential. The temperature is considered to be periodically oscillating with $T(t)<T_c$, where T_c is the transition temperature below which symmetry of the theory spontaneously broken. Due to $T^2\Phi^2$ term, minima of the effective potential periodically oscillates. These oscillations induce field excitations (dominantly longitudinal excitations) via the *parametric res-*

onance of the field. The parametric resonance occurs when the frequency of temperature oscillations matches with the mass of the field. These excitations ultimately lead to the formation of vortex-antivortex pairs in U(1)-theory [7] and kink-antikink pairs in \mathcal{Z}_2 -theory [8].

In Bose-Einstein condensate (BEC) of trapped ultracold atoms, a new mechanism of formation of superfluid vortices has been studied in refs.[9, 10]. In these studies, vortex-antivortex pairs are generated by periodically varying trapping potential of BEC condensate. Note that the dynamics of superfluid is governed by the time-dependent Gross-Pitaevskii equation (GPE), solution of which gives a coherent wavefunction of BEC condensate [11]. These studies suggest that under the perturbation, time dependent excitations arise in the condensate modifying the coherent wavefunction. These excitations lead to the formation of vortex-antivortex pairs in the system. Subsequently, a tangled network of vortices forms in the system signalling transition to a state of quantum turbulence. Ultimately, BEC condensate reaches a disordered state. In these studies, the oscillation frequency of trapping potential is taken 200 Hz, and the time scale for the whole process is few tens of millisecond. Note that this time scale depends upon the amplitude and frequency of oscillations of trapping potential (i.e. rate of injected energy) and the energy of the vortex configuration in the system.

Following the above studies in refs.[7–10], it is an obvious question to ask if spacetime oscillations can also induce parametric resonance or large oscillations in the field Φ . Such a question is relevant for many systems, for example ultralight axion-like field coupled to gravitational waves, neutron star superfluidity under time dependent tidal deformations, etc. The dynamical and thermal evolution of a neutron star, in terms of periodic glitches and cooling rate respectively, strongly support the existence of neutron superfluidity in the interior re-

gions of star [12, 13]. The theoretical studies suggest the presence of 1S_0 neutron superfluidity in the inner crust region, while 3P_2 neutron superfluidity as well as 1S_0 proton superconductivity in the outer core region [13]. In the inner core region there is also possibility of existence of *color superconducting phases* of quantum chromodynamics (QCD) [14]. During a binary neutron stars (BNS) merger, the orbiting neutron stars exert a time dependent tidal force on each other [15]. The frequency and amplitude of this tidal force keep on increasing with time, and become maximum towards the end of merger. Under such tidal force, depending upon the *tidal deformability*, neutron star undergoes a time dependent deformations. These tidal deformations can couple to the condensate of interior superfluid of neutron star and may lead to the turbulence (formation of tangled vortices) as discussed in refs.[9, 10]. Here, we mention that a similar kind of scenario, e.g. occurrence of superfluid turbulence, superfluid to normal fluid transition, and glitch (or anti-glitch) in neutron stars during a BNS merger has been discussed in ref.[16].

Note that due to the tidal force during the merger, energy pumped into the system is so high that the (local) temperature and density of neutron stars can reach up to 100 MeV and few times of nuclear saturation density, respectively [17]. In such a situation neutron superfluidity can be destroyed (in some local regions) even before the completion of merger as the transition temperature for such superfluidity lies somewhere in between 0.1 MeV to 5 MeV [18]. Therefore the generation of excitations, vortex-antivortex pairs, and quantum turbulence in superfluid condensate during the merger are expected to occur in the intermediate stage of evolution of neutron stars. This may also be possible, that the condensate excitations become so high that the neutron stars superfluidity destroys even before reaching the transition temperature (as discussed in studies [9, 10]). Certainly, the superfluid phase of quark matter (e.g. color-flavor locked phase) in the inner core of neutron stars can survive for a longer time as it has transition temperature ~ 100 MeV [14].

In order to study the time evolution of superfluid inside neutron star under such time dependent tidal deformation, one must solve the relativistic Gross-Pitaevskii equation, known as the Gross-Pitaevskii-Anandan equation [19], in the background of spacetime metric of star with a time dependent perturbation appropriate for the BNS merger system. This study can also be done by solving non-linear Klein-Gordon equation in an appropriate metric background, as superfluidity can also be described in the field theoretical framework, where BEC is generally characterized by spontaneous breaking of U(1) global symmetry for a complex scalar field $\Phi = \Phi_0 e^{i\theta}$ [20, 21]. In this description, the condensate density ρ_s is related with the vacuum expectation value (VEV) of the field as $\rho_s = \Phi_0^2 / \xi_s$, where ξ_s is the correlation length [21]. A

spatial variation of phase θ of the field gives flow to the superfluid. The metric oscillations mentioned above may generate excitations in the field Φ and lead to the formation of vortex-antivortex pairs in the interior superfluid of neutron star.

In this paper, we study the effects of spacetime oscillations on the evolution of a complex scalar field. This may shade some light on the time dynamics of interior superfluidity of neutron star during the merger. However, in this work we are not doing phenomenology of any particular system. Rather, the present work is completely formal, where we show for the first time that how a complex scalar field gets excited and topological vortices form under the spacetime oscillations. Therefore, here, instead of considering a spacetime metric of star, for simplicity we take Minkowski metric with a periodic perturbation in time. This simplification helps to give a clear understanding of the effect of metric oscillations on the field and production of topological vortices. In this metric background, we numerically solve the non-linear Klein-Gordon equation in (2+1)-dimensions for the time evolution of a complex scalar field with an initial field configuration given by, $\Phi(x, y) = \Phi_0 + \delta\Phi(x, y)$, where Φ_0 is the VEV of U(1)-broken effective potential and $\delta\Phi(x, y)$ represents small fluctuations of field about the VEV. Here, the initial field fluctuations are considered, as the spacetime oscillations couple with the field equation only through the spacetime derivatives of the field; see equation of motion below.

We see that under the spacetime oscillations, field undergoes large amplitude oscillations for a wide range of frequencies of spacetime oscillations, which eventually leads to the formation of vortex-antivortex pairs. In the low frequency regime (frequency smaller than the mass of field) mainly transverse modes (Goldstone modes) arise, while in the high frequency regime, longitudinal modes also get generated dominantly. A detailed analysis shows that there is a correspondence between the frequency of spacetime oscillations and momentum of time growing field-modes. This suggests that the field undergoes *parametric resonance* under the spacetime oscillations.

We mention that our present study is fundamentally different from the previous studies in refs.[7, 8], even though the underlying physics for the generation of topological defects is same, i.e. *parametric resonance*. In previous studies oscillating temperature couples to the magnitude of the field. Therefore, in order to observe parametric resonance, the frequency of temperature oscillations must be close to the mass of longitudinal modes of the field. In present case, the spacetime oscillations couple to the gradient of the field. This makes a direct coupling between the frequency of spacetime oscillations to the momentum of field-modes present in the initial field configuration. Therefore by satisfying the resonance condition, some specific field-modes grow exponentially with time. This can occur, as far as the appropriate

momentum-modes of the field are present in the system. Thus, in present case mass of the field doesn't set the lowest frequency cut-off to induce parametric resonance, hence vortex-antivortex pairs could be formed for a wide range of frequencies of spacetime oscillations. Rather, for this phenomena, the lowest frequency cut-off is set by the system size due to finite size effects. Our results suggest that the frequency of spacetime oscillations must be greater than $2/(\text{system size})$ to induce the parametric resonance of the field.

In the case of neutron stars during BNS merger, the accessible frequencies of spacetime oscillations are many orders of magnitude smaller than the mass of the condensate field of interior superfluidity ($\sim 0.1 - 5.0$ MeV). Therefore in this case, even the transverse excitation of condensate field may get difficulties to generate due to finite size effects. Our present results suggest that in a typical neutron star of radius ~ 10 km, to generate condensate excitations, the frequency of spacetime oscillations must be greater than ~ 30 kHz. This required frequency is way beyond the reach of any known BNS merger systems, which could generate maximum frequency of spacetime oscillations up to ~ 1 kHz. Therefore, it is difficult to generate condensate excitations of neutron star superfluidity, under the phenomena of parametric resonance, during BNS merger.

However, this has to be investigated in detail that whether there is any other method by which condensate excitation in neutron star superfluidity can be generated during mergers. We mention that in the case of BEC of ultracold atoms, 200 Hz frequency of oscillations of trapping potential is sufficient to excite the condensate with system size of only few hundred micrometer in few ten millisecond time [9]. Therefore, it is not very unrealistic to expect the generation of such condensate excitations and formation of vortex-antivortex pairs in the interior superfluidity of neutron star during BNS merger. This requires a detailed investigation, which we will try to pursue in future.

This paper is organized as follows. In section-II, we derive the equation of motion for a complex scalar field in the presence of oscillating spacetime metric background. In section-III, we outline the details of our numerical simulations. Then we present our simulation results in section-IV. Finally, we briefly summarize our work and give future outlook in section-V.

II. EQUATION OF MOTION

In order to study the effects of spacetime oscillations on a complex scalar field, we consider the spacetime metric as a periodic perturbation on the top of the Minkowski metric. We consider the *inverse* spacetime metric as, $g^{\mu\nu} \equiv \text{diag}(-1, 1 - \varepsilon \sin(\omega(t-z)), 1 + \varepsilon \sin(\omega(t-z)), 1)$,

where $\varepsilon (< 1)$ and ω are the amplitude and frequency of spacetime oscillations, respectively; (t, x, y, z) are spacetime coordinates. Note that this form of the metric is chosen just for a simplicity in the equation of motion of the field, though any periodic time-dependent metric can be taken for our study. The action of the complex scalar field on the spacetime manifold with the above metric is [21, 22],

$$S = \int d^4x \sqrt{-g} \left[-\frac{1}{2} g^{\mu\nu} \partial_\mu \Phi^* \partial_\nu \Phi - V(\Phi^* \Phi) \right], \quad (1)$$

where, $g = \det(g_{\mu\nu}) = -(1 - \varepsilon^2 \sin^2(\omega(t-z)))^{-1}$, $\Phi = \phi_1 + i\phi_2$, $\Phi^* = \phi_1 - i\phi_2$; ϕ_1 and ϕ_2 are the real scalar fields. We consider the following symmetry breaking effective potential,

$$V(\Phi^* \Phi) = \frac{\lambda}{4} (\Phi^* \Phi - \Phi_0^2)^2, \quad (2)$$

where, λ is the self-interaction coupling parameter of the field, and Φ_0 is the VEV of the effective potential. With this, $m_\Phi = \Phi_0 \sqrt{2\lambda}$ is the mass of the longitudinal component of the field. The equation of motion for (ϕ_1, ϕ_2) fields are [21, 22],

$$\square \phi_i - \frac{dV}{d\phi_i} = 0, \quad (3)$$

where, $i = 1, 2$. The covariant d'Alembertian is given by,

$$\square \phi_i = \frac{1}{\sqrt{-g}} \partial_\mu (\sqrt{-g} g^{\mu\nu} \partial_\nu \phi_i). \quad (4)$$

Therefore in the expanded form, the field equations are,

$$\begin{aligned} & -\frac{1}{2} \frac{\varepsilon^2 \omega \sin(2\omega(t-z))}{(1 - \varepsilon^2 \sin^2(\omega(t-z)))} \left(\frac{\partial \phi_i}{\partial t} + \frac{\partial \phi_i}{\partial z} \right) - \frac{\partial^2 \phi_i}{\partial t^2} \\ & + (1 - \varepsilon \sin(\omega(t-z))) \frac{\partial^2 \phi_i}{\partial x^2} + (1 + \varepsilon \sin(\omega(t-z))) \frac{\partial^2 \phi_i}{\partial y^2} \\ & + \frac{\partial^2 \phi_i}{\partial z^2} - \lambda \phi_i (\phi_1^2 + \phi_2^2 - \Phi_0^2) = 0. \end{aligned} \quad (5)$$

For the simplicity of solving it numerically, (i) we assume that there is no variation of the field Φ along z -direction, and (ii) we look at the solution of the field only in the $z=0$ plane. With these simplifications, the above equations reduce to,

$$\begin{aligned} & -\frac{1}{2} \frac{\varepsilon^2 \omega \sin(2\omega t)}{(1 - \varepsilon^2 \sin^2(\omega t))} \frac{\partial \phi_i}{\partial t} - \frac{\partial^2 \phi_i}{\partial t^2} + (1 - \varepsilon \sin(\omega t)) \frac{\partial^2 \phi_i}{\partial x^2} \\ & + (1 + \varepsilon \sin(\omega t)) \frac{\partial^2 \phi_i}{\partial y^2} - \lambda \phi_i (\phi_1^2 + \phi_2^2 - \Phi_0^2) = 0. \end{aligned} \quad (6)$$

It is very clear from the above equations, that the spacetime oscillations only couple to the derivatives of the

field. Note that in the equations, the coefficient of first order time derivative has oscillations with a mixture of frequencies ω and 2ω . Under the spacetime oscillations, gradient of the field oscillates, which must induce oscillations in the field via the *parametric resonance* with different possible oscillation frequencies. These field oscillations must be modulated by the steep rise of the effective potential in the longitudinal direction. The parametric resonance of the field eventually leads to the formation of vortex-antivortex pairs in the system. Our simulation results validate these expectations, which we present in the following sections.

III. SIMULATION DETAILS

To perform the simulation, we discretize the xy -plane into 200×200 lattice points with the lattice spacing of $\Delta x = \Delta y = 0.01 \Lambda$, giving the total lattice size of 2.0Λ in each direction (here, Λ is a unit of length and time, which we haven't specified, as in this work we are not giving phenomenological prediction for any system). Δx and Δy should be smaller than inverse of the field-mass, i.e. $\Delta x, \Delta y < m_{\Phi}^{-1}$, so that a reasonable spatial variation of the field can be resolved. The time is discretized in the time step of $\Delta t = 0.005 \Lambda$. Note that in the equation of motion (Eq.(6)), the discretization in the time-axis works only if the condition $\Delta t < \omega^{-1}$ satisfies. In our simulation, we study the effects of spacetime oscillations, in particular, the role of parameters ε and ω on the field evolution. To describe the effects, for most of the simulations, we consider $\varepsilon = 0.4$ and $\omega = 100 \Lambda^{-1}$. We take the parameters of the effective potential as $\Phi_0 = 10 \Lambda^{-1}$ and $\lambda = 40$. We also point out how the results vary with these parameters.

In Eq.(6), the field evolution is coupled with spacetime oscillations through second order spatial derivative and first order time derivative of the field. Therefore initial field configuration can respond to the spacetime oscillations only when fluctuations of the field (spacetime gradient) be present in the system (i.e. iff the field configuration is not in its complete minimum energy configuration), which can naturally arise due to the presence of thermal and/or quantum fluctuations. For simplicity, we consider fluctuations only in the initial field configuration, i.e. we take $\Phi(x, y) = \Phi_0 + \delta\Phi(x, y)$ at time $t = 0$ and evolve with Eq.(6).

In our simulation, for the initial field configuration, we have considered small spatial variations in ϕ_1 and ϕ_2 fields such that the magnitude remains Φ_0 , i.e. the field is taken at the minima of the effective potential (Eq.2) and only transverse fluctuations of the field has been considered for the simulation. However, we have seen that considering fluctuations in the magnitude of the field doesn't change any qualitative aspect of the simulation results. More specif-

ically, we have taken $\phi_1(x, y, t=0) = \Phi_0 \sqrt{1 - \alpha_{xy}^2}$ and $\phi_2(x, y, t=0) = \Phi_0 \alpha_{xy}$, where α_{xy} varies randomly from point to point on the lattice in the range $[-\beta, \beta]$; here $0 < \beta \ll 1$. This initial field configuration has a non-zero spatial gradient of both the fields. In our simulation, we have taken $\beta = 0.2$. However, we have seen that choosing different β doesn't change results qualitatively. We evolve this initial field configuration by solving Eq.(6) using second order Leapfrog method, and considering periodic boundary condition along the spatial directions.

IV. SIMULATION RESULTS

A. Parametric resonance of field under spacetime oscillations

We now present our simulation results. In Fig.1, we have shown the vector plots of field configuration in the physical space (xy -plane) at four different times. The x - and y -components of the vector field correspond to ϕ_1 and ϕ_2 fields, respectively. Note that the whole lattice area is $2.0 \times 2.0 \Lambda^2$, but we have shown only a small portion of the lattice. In this simulation, we have taken $\varepsilon = 0.4$, $\omega = 100 \Lambda^{-1}$, $\Phi_0 = 10 \Lambda^{-1}$, and $\lambda = 40$. As we have mentioned earlier, we take random transverse fluctuations in the initial field configuration, therefore phase of the field varies randomly from one lattice point to other within the range of $\pm 0.2 \text{ rad}$ for the given value of β . Fig.1(a) corresponds to the initial field configuration (at time $t=0$), where one can see such phase fluctuations on the lattice points. We observe that roughly during the time interval of $0.5 - 1.5 \Lambda$, the field itself starts performing spacetime oscillations with a significantly large amplitude; at time larger than this, field dynamics becomes much more complicated. Fig.1(b) shows the field configuration at time $t=1.3 \Lambda$. This figure clearly shows that there is generation of a systematic periodic variation (waves) of the field in the physical space. The amplitude of these waves increases with time. We observe that the wavelength of these waves is ω dependent; by decreasing ω , the wavelength of these waves increases (see Fig.4 and Fig.5 in this regard). Depending upon the choice of ω , these waves may contain the longitudinal excitation along with transverse excitation of the field. Due to the generation of these excitations, the field acquires a significant energy in some parts of the physical space to climb the central barrier of the effective potential and fall into the opposite side of the vacuum manifold. This leads to the formation of vortex-antivortex pairs in the system. This process can be seen in Fig.1(c) and Fig.1(d) which are plotted at time $t=1.7 \Lambda$ and $t=1.8 \Lambda$, respectively. The vortex-antivortex pairs appear and disappear in the system, and the overall number of pairs keeps on increasing with time. Roughly at the time $t=2.5 \Lambda$, fluctuations

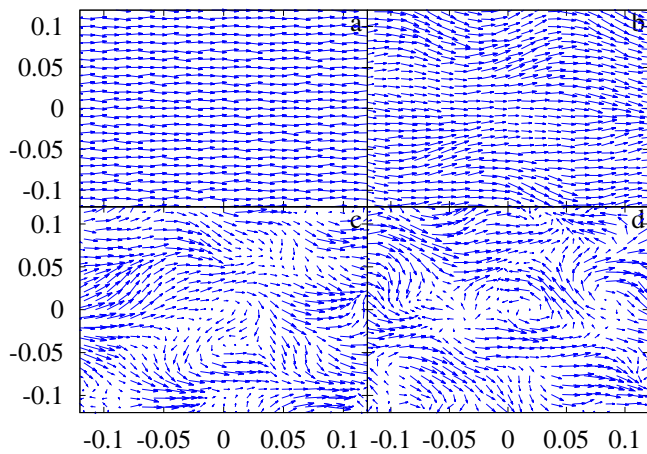


FIG. 1: Figure shows the vector plots of field configuration in physical space (xy -plane) at four time steps of field evolution. The parameters of simulation are $\varepsilon=0.4$, $\omega=100 \text{ \AA}^{-1}$, $\Phi_0=10 \text{ \AA}^{-1}$, $\lambda=40$. Plots (a),(b),(c), and (d) correspond to the field configurations at time $t=0$, 1.35, 1.7, and 1.8 \AA , respectively. In plot(d) vortex-antivortex pairs has been formed. Roughly at time $t=2.5 \text{ \AA}$ field configuration achieves a *disordered state*.

become so strong, that the field configuration no longer remains in the *ordered state* and achieves a *disordered state* (not shown in the figure).

In Fig.2, we have plotted distribution of the field in the $\phi_1\phi_2$ -plane (field-space) at four different times. (In this figure, the field has been mapped from the physical space to the field-space.) The density of points is indicated by colors in the figure. The parameters of simulation are same as used in Fig.1. Fig.2(a) shows the field distribution at time $t=0.05 \text{ \AA}$, which has a highly localized distribution around $\phi_1 \approx \Phi_0 = 10 \text{ \AA}^{-1}$ and $\phi_2 \approx 0$ due to our choice of initial field configuration. In Fig.2(a), the maximum height of the distribution is 2672. Note that we have normalized the distribution such that in each case the density varies between 0 and 1. As field evolves, the distribution keeps on spreading around the initial distribution in the field-space. Fig.2(b) shows the field distribution at time $t=1.05 \text{ \AA}$ with maximum distribution height of 316. One can clearly see that at this time, mostly the transverse excitation has been generated. Fig.2(c) shows the stage of field distribution at time $t=1.35 \text{ \AA}$ with distribution height of 88. By this time, both kind of excitations, transverse as well as longitudinal, have been generated in the system. Note that Fig.2(b) and Fig.2(c) correspond to the time duration in which field oscillates with a significantly large amplitude, as shown in Fig.1(b). These excitations ultimately leads to the formation of vortex-antivortex pairs in the system. The field distribution, at the time stage when these pairs have been formed, is shown in Fig.2(d) at time $t=1.8 \text{ \AA}$ with maximum distribution height of 26. Subsequently, the field distribution spreads over the field-space symmet-

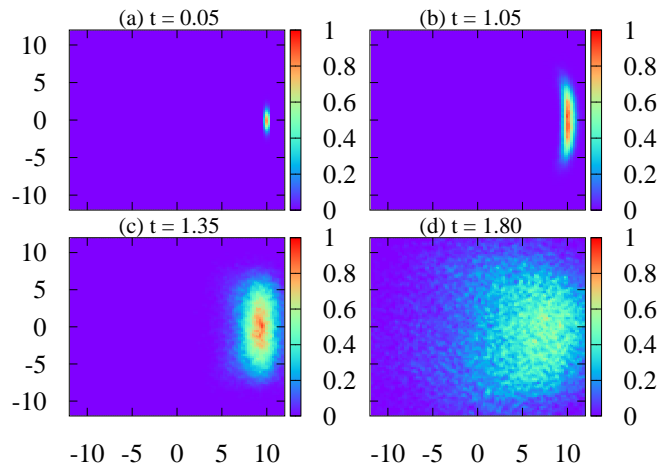


FIG. 2: In the figure, we have plotted distribution of field in the field-space ($\phi_1\phi_2$ -plane) at four different times of field evolution. Note that we have normalized the distribution such that each density plot gets variation in between 0 and 1. Plots (a),(b),(c), and (d) correspond to time steps $t=0.05$, 1.05, 1.35, and 1.8 \AA , respectively. In plot(a), field distribution is highly localized about the chosen minima of the effective potential, which becomes more spread in plot(b), where mostly transverse excitation has been generated. In plot(c) longitudinal excitation also has been generated. At the time stage of plot(d), field flips to the opposite side of the effective potential leading to the formation of vortex-antivortex pairs.

rically around $\phi_1=\phi_2=0$, the maximum extent of which becomes way beyond Φ_0 signalling a *disordered state* of the field.

To see how fluctuations in fields ϕ_1 and ϕ_2 grow with time, we calculate field's fluctuations $\delta\phi_i(t)=\sqrt{\langle\phi_i^2(\vec{x},t)\rangle-\langle\phi_i(\vec{x},t)\rangle^2}$, where $i=1,2$, and bracket $\langle\dots\rangle$ represents the volume average of the field. Fig.3 shows the time evolution of $\delta\phi_1$ and $\delta\phi_2$ for two sets of parameters of the effective potential. The parameters of spacetime metric for the simulations are $\varepsilon=0.4$ and $\omega=100 \text{ \AA}^{-1}$, same as used in Figs.1,2. Plots (a)(blue) and (b)(gray) are the time evolution of $\delta\phi_1$ and $\delta\phi_2$ for $\Phi_0=10 \text{ \AA}^{-1}$ and $\lambda=40$, while plots (c)(black) and (d)(red) are the time evolution of $\delta\phi_1$ and $\delta\phi_2$ for $\Phi_0=0.1 \text{ \AA}^{-1}$ and $\lambda=4$, respectively. Note that ϕ_1 and ϕ_2 at initial time are proportional to Φ_0 , that is the reason due to which $\delta\phi_1$ and $\delta\phi_2$ start with larger values in plots (a) and (b) in comparison with plots (c) and (d) even though the chosen value of β for both the sets of parameters of the effective potential are the same (indeed, the fluctuations in phase of field are same for both the sets of parameters of the effective potential). Figure clearly shows that in each case, the growth of fluctuation in ϕ_2 field is larger than fluctuation in ϕ_1 . This depends upon our choice of initial field configuration. After some time, both the field fluctuations become degenerate. Note that there are oscillations in plots (a) and (b) during the time interval of 0.5 - 1.5 \AA . These oscillations

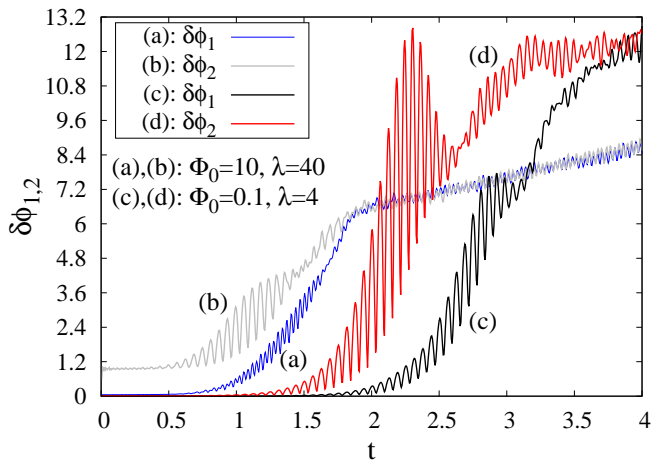


FIG. 3: Figure shows the time evolution of growth of fluctuations $\delta\phi_1$ and $\delta\phi_2$ of fields ϕ_1 and ϕ_2 , respectively, under the spacetime oscillations for two sets of parameters of the effective potential. The parameters of spacetime metric are $\varepsilon=0.4$ and $\omega=100 \Lambda^{-1}$. Plots (a)(blue) and (b)(gray) are the time evolution of $\delta\phi_1$ and $\delta\phi_2$ for $\Phi_0=10 \Lambda^{-1}$ and $\lambda=40$, while plots (c)(black) and (d)(red) are for $\Phi_0=0.1 \Lambda^{-1}$ and $\lambda=4$, respectively. Figure clearly shows that in each case, the initial growth of $\delta\phi_2$ is larger in comparison with $\delta\phi_1$; both, $\delta\phi_1$ and $\delta\phi_2$, ultimately become degenerate. Note that there are oscillations in plots (a) and (b) during the time interval of 0.5 - 1.5 Λ . These oscillations correspond to the field oscillations discussed in Fig.1.

correspond to the large amplitude *field oscillations* as discussed in Fig.1.

We now discuss a very crucial issue regarding the properties of formed vortices at different frequency regimes of spacetime oscillations. For two sets of parameters of the effective potential in Fig.3, the mass of the field m_Φ are $89.44 \Lambda^{-1}$ and $0.28 \Lambda^{-1}$, respectively. Therefore, with used ω in this figure, for former case $m_\Phi < \omega < 2m_\Phi$, while for latter case $\omega \gg m_\Phi$. Even though in both the cases there are qualitative similar growths in the fluctuations, there is a basic difference in the evolution of the field for these two cases. In the case of $\omega \gg m_\Phi$, spacetime oscillations generate waves in the field configuration having much shorter wavelength in comparison with m_Φ^{-1} (spacetime oscillations generate transverse-modes with momentum $\approx \omega/2$; see details later). Further, later we have shown that under the spacetime oscillations, the longitudinal-modes of the field also grow along with transverse-modes following the relation $|\vec{k}|^2 + m_\Phi^2 = (\frac{n\omega}{2})^2$, where $|\vec{k}|$ is the momentum of the longitudinal-modes of the field, and $n=1,2,3,\dots$. Therefore in the case of $\omega \gg m_\Phi$, the fastest growing longitudinal-modes ($n=1$ and/or $n=2$) must have much larger momentum in comparison with m_Φ . All this leads huge excitations in the field for $\omega \gg m_\Phi$, and the field acquires value much larger than VEV in a short time. In such situation, the field doesn't feel the presence of central barrier of effective po-

tential and does back and forth across this easily. Now, as the core size of a topological vortex is given by m_Φ^{-1} where the field magnitude at distances larger than m_Φ^{-1} is given by VEV, therefore under such a huge field excitations having much shorter wavelength in comparison with m_Φ^{-1} , there is no any possibility of formation of vortices which satisfy the properties of topological vortices. Thus, in the case of $\omega \gg m_\Phi$, topological vortices cannot be formed under the spacetime oscillations. Note that for second set of parameters of the effective potential, our lattice size is lesser than m_Φ^{-1} , hence it cannot accommodate even a single topological vortex for these parameters, however our above conclusion is true even for a lattice which is much bigger than m_Φ^{-1} .

However, we mention that in this case with sufficient evolution of the field, i.e. after time $t \simeq 2.7 \Lambda$, we see some vortex-antivortex kind of structures (even on the used lattice), though these are not topological vortices. In these vortices, due to huge excitations, the field acquires values way beyond the VEV outside the vortex core; note that in this case, VEV is $0.1 \Lambda^{-1}$, where outside these vortices, at this time field acquires value $\simeq 20 \Lambda^{-1}$, which is 200 times larger than VEV. Also, in this case the vortex core size, we have found to be given by $\sim \omega^{-1}$ (instead of m_Φ^{-1}), as expected from the wavelength of the generated field excitations. Thus, these vortices certainly don't satisfy the properties of topological vortices, rather their properties are determined by the parameters of spacetime oscillations. Basically in this case, the magnitude of the field becomes so large in comparison with VEV that field configuration enables to create vortices (non-topological) with core size of much shorter length scale than m_Φ^{-1} . (To see the vortices in the case of $\omega \gg m_\Phi$, we refer reader to see Fig.14, where $m_\Phi=0.28 \Lambda^{-1}$ and $\omega=17 \Lambda^{-1}$ has been used for the simulation).

On the other hand, in the former case as discussed above, although longitudinal excitation arises and hence vortices are not well formed, vortices up to some extent satisfy the properties of topological vortices; see Fig.1 and Fig.2. Later, we have also shown that there is a fundamental difference in the evolution of field for $\omega > m_\Phi$ and for $\omega \leq m_\Phi$. In the case of $\omega \leq m_\Phi$, the field remains close to VEV where mainly transverse excitation arises under the spacetime oscillations. Therefore, the formed vortices in such case are also topological vortices; see Fig.10. Thus, only in the cases where spacetime oscillation frequency is either lesser than or close to the mass of the field, i.e. only when $\omega \lesssim m_\Phi$, the formed vortices under these oscillations are topological in nature. In our simulations, however, the field-profile of these vortices never achieve an exact profile of topological vortices as the field configuration has to bear continuous spacetime oscillations.

In order to further investigate the behavior of field configurations at various time stages, we calculate the time evolution of various momentum-modes of the fields ϕ_1

and ϕ_2 . The Fourier transform of the field configuration from the physical space to the momentum space at any time is given by,

$$\tilde{\phi}_i(\vec{k}, t) = \frac{1}{\mathcal{A}} \int_{b.c.} d^2\vec{x} \phi_i(\vec{x}, t) e^{i\vec{k}\cdot\vec{x}}; \quad i = 1, 2, \quad (7)$$

where \mathcal{A} is the total area of the system, *b.c.* stands for the *boundary condition*, and $\vec{k}=k_x\hat{x}+k_y\hat{y}$, $\vec{x}=x\hat{x}+y\hat{y}$ are the momentum and position vectors, respectively. In Fig.4 and Fig.5, we have plotted modulus of momentum-modes of fields ϕ_1 and ϕ_2 , i.e. $|\tilde{\phi}_1(\vec{k}, t)|$ (upper panel) and $|\tilde{\phi}_2(\vec{k}, t)|$ (lower panel), in the momentum space with spacing $\Delta k_x=\Delta k_y=2.0 \Lambda^{-1}$. In Fig.4, we have taken spacetime oscillation frequency larger than m_Φ , while in Fig.5, frequency is taken smaller than that. Therefore the field dynamics is expected to be different in both the cases. (The white regions in plots correspond to the magnitude larger than the maximum range of legends.) Note that for ϕ_1 field, zero-mode (zero-momentum mode) is the most dominant mode, while for ϕ_2 , zero-mode is very close to zero. This is just because of initially chosen values of these fields. In Fig.4, we have taken $\omega=100 \Lambda^{-1}$, $\varepsilon=0.4$, $\Phi_0=10 \Lambda^{-1}$, $\lambda=40$ for the simulation. From left to right, field-modes are plotted at time $t=0.05, 1.05, 1.35, 1.8 \Lambda$; see Fig.1 and Fig.2 also. Note that the time interval of $0.5 - 1.5 \Lambda$ is the time-stage of large amplitude oscillations of the field for the given ω . At the initial time itself, all higher momentum-modes of the field up to $k_x=k_y=2\pi/\Delta x$ are present due to the prescribed random fluctuations, which can be seen in the plot at time $t=0.05 \Lambda$. Under the spacetime oscillations, depending upon the frequency ω , some specific momentum-modes of field grow with time. In the figure, there are noticeable growth of $|\tilde{\phi}_1(\vec{k}, t)|$ at $k_x=15 \Lambda^{-1}$, $k_y=\omega$ and $k_x\approx k_y\approx\sqrt{(\omega^2 - (\frac{m_\Phi}{\sqrt{2}})^2)/2} = 54.77 \Lambda^{-1}$, and growth of $|\tilde{\phi}_2(\vec{k}, t)|$ at $k_x=0$, $k_y=\omega/2$ and $k_x=\omega/2$, $k_y=0$. The subsequent evolution also leads to the growth of various other momentum-modes of both the fields.

In Fig.5, we have taken $\omega=50 \Lambda^{-1}$, $\varepsilon=0.4$, $\Phi_0=10 \Lambda^{-1}$, $\lambda=40$ for the simulation. From left to right, field-modes are plotted at time $t=2.0, 2.5, 3.0, 3.5 \Lambda$. In this case also, the initial distributions of field-modes are same as plotted in Fig.4 at time $t=0.05 \Lambda$ (therefore, not shown again in Fig.5). Note that for the given ω , the time interval of $2.0 - 3.7 \Lambda$ corresponds to the large amplitude oscillations of the field. Figure clearly shows that there are noticeable growth of $|\tilde{\phi}_1(\vec{k}, t)|$ at $k_x=0$, $k_y=\omega$, and growth of $|\tilde{\phi}_2(\vec{k}, t)|$ at $k_x=0$, $k_y=\omega/2$. In the intermediate stage of field evolution, there are also growth of $|\tilde{\phi}_1(\vec{k}, t)|$ at $k_x\approx\omega/2$, $k_y\approx\omega/2$ and $k_x\approx\omega/2$, $k_y\approx 3\omega/2$. In this case also, the subsequent evolution leads to the growth of various other momentum-modes of both the fields.

To understand why some specific momentum-modes of the field grow for a given ω , we write the field as $\Phi=\Phi_0+v_1+iv_2$ ($\phi_1=\Phi_0+v_1$, $\phi_2=v_2$), where v_1 and v_2 are

small fluctuations of the field about the VEV. We write the equation of motion for these fluctuations keeping term up to linear order in these fields, and then Fourier transform in the momentum space. The evolution equations for momentum-modes of these fluctuations are,

$$\frac{\varepsilon^2\omega \sin(2\omega t)}{2 f(t) f(-t)} \dot{\tilde{v}}_{ik} + \ddot{\tilde{v}}_{ik} + (k_x^2 f(t) + k_y^2 f(-t) + m_i^2) \tilde{v}_{ik} = 0, \quad (8)$$

where $\tilde{v}_{ik}\equiv\tilde{v}_i(\vec{k}, t)$, $f(t)=(1-\varepsilon \sin(\omega t))$, $m_1=m_\Phi$, and $m_2=0$. These equations clearly show that \tilde{v}_{1k} and \tilde{v}_{2k} undergo parametric resonance (get resonant growth) if suitable conditions (relations between k_x , k_y , m_i , and ω) are satisfied. We numerically solve these equations and find that there are various resonance conditions for both the fields. In a reasonable range of frequency ω , the resonance conditions for \tilde{v}_{ik} are $|\vec{k}|^2+m_i^2=(\frac{n\omega}{2})^2$, where $n=1,2,3,\dots$. For each n , there are different frequency cut-off for \tilde{v}_{1k} to get resonance growth, which are $\omega\leq 2m_\Phi/n$. This indicates that the most dominant modes of \tilde{v}_{1k} , i.e. modes for $n=1$ and $n=2$, don't grow when ω becomes close to or lesser than m_Φ . Thus, effectively the frequency cut-off for the longitudinal-modes is $\omega\leq m_\Phi$. While for \tilde{v}_{2k} , there is no such frequency cut-off (due to its zero mass), therefore it can undergo parametric resonance even for any low frequency ω (where $\omega>0$). For a comparison, if one ignores the first term from the equation of \tilde{v}_{2k} , then in (1+1)-dimensions it takes the form of the *harmonic oscillator equation* with the (time dependent) frequency square $k_{x(y)}^2(1\mp\sin(\omega t))$ [23]. In such case, the oscillator undergoes *parametric resonance* when the condition $k_{x(y)}\simeq n\omega/2$ satisfies [23]. For the given frequency ω , the growth rates of growing modes of \tilde{v}_{ik} are different, which become changed for different ω . The fastest growing modes, out of \tilde{v}_{1k} and \tilde{v}_{2k} , are \tilde{v}_{2k} at $k_{x(y)}=\omega/2$, $k_{y(x)}=0$, whose growth rates decrease by decreasing frequency of spacetime oscillations. This response of field-modes to the frequency ω can be important in the understanding of time of formation of first vortex-antivortex pair in the system at different frequencies ω .

A similar feature of the resonance can be seen in Fig.4 and Fig.5, where $\tilde{\phi}_2$ grows resonantly at $k_{x(y)}\simeq\omega/2$, $k_{y(x)}\simeq 0$. In these figures there is a qualitative difference in the evolution of $\tilde{\phi}_1$ for $\omega>m_\Phi$ and $\omega<m_\Phi$, as for $\omega>m_\Phi$ some momentum-modes of the longitudinal component (\tilde{v}_{1k}) also grow resonantly. This makes clear that in the frequency regime $\omega>m_\Phi$, both components of the field, longitudinal as well as transverse, participate in the resonance process equally, while in the frequency regime $\omega\leq m_\Phi$ mainly transverse component. This has to be noted that in Fig.4, $\tilde{\phi}_1$ grows by following relation $|\vec{k}|^2+(\frac{m_\Phi}{\sqrt{2}})^2=\omega^2$, instead of following relation obtained for \tilde{v}_{1k} at $n=2$. This happens probably because ϕ_1 is the field whose values are given from the center of the effective potential. This is important to appreciate that the

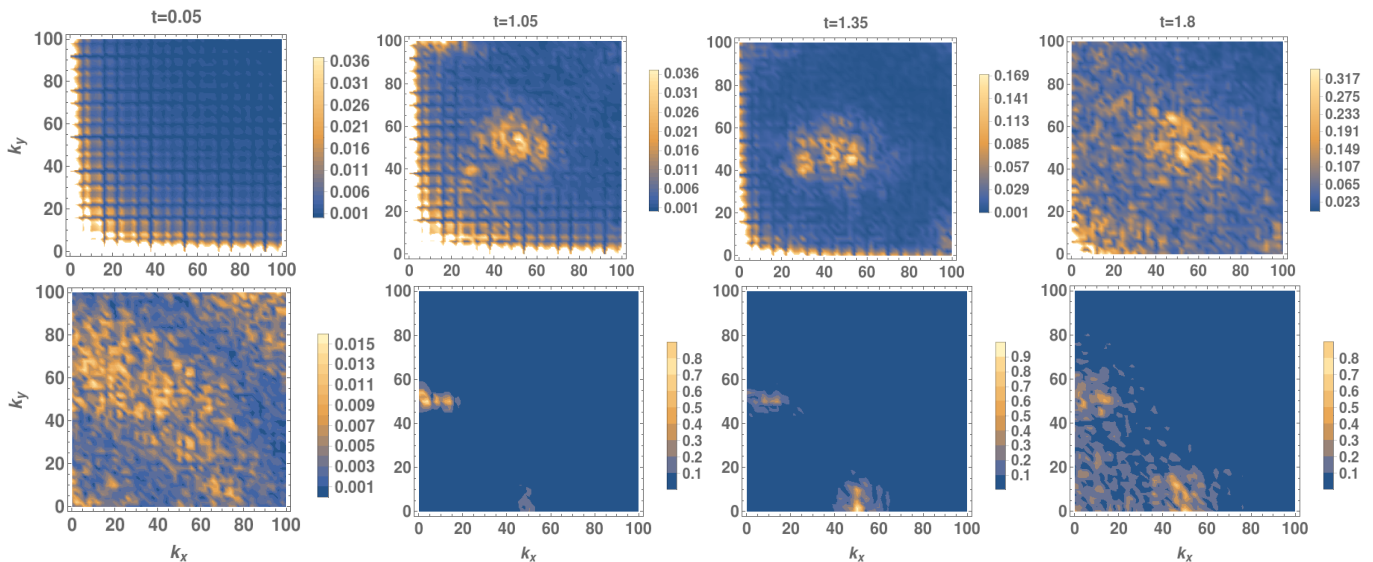


FIG. 4: Figure shows the profile of modulus of field-modes $|\tilde{\phi}_1(\vec{k}, t)|$ (upper panel) and $|\tilde{\phi}_2(\vec{k}, t)|$ (lower panel) at different times for $\omega=100 \text{ \AA}^{-1}$, $\varepsilon=0.4$, $\Phi_0=10 \text{ \AA}^{-1}$, $\lambda=40$. From left to right, modes are plotted at time $t=0.05, 1.05, 1.35, 1.8 \text{ \AA}$. There are noticeable growth of $|\tilde{\phi}_1(\vec{k}, t)|$ at $k_x=15 \text{ \AA}^{-1}$, $k_y=\omega$ and $k_x \approx k_y \approx \sqrt{(\omega^2 - (\frac{m\Phi_0}{\sqrt{2}})^2)/2} = 54.77 \text{ \AA}^{-1}$, and growth of $|\tilde{\phi}_2(\vec{k}, t)|$ at $k_x=0$, $k_y=\omega/2$ and $k_x=\omega/2$, $k_y=0$. The subsequent evolution also leads to the growth of various other momentum-modes of both the fields.

appropriate momentum-modes of the field corresponding to ω has to be present initially, otherwise resonance will not occur. Thus, under the spacetime oscillations, there is no frequency cut-off for resonance to occur as far as the appropriate momentum-modes of the field are present to grow (however, finite size effects of system set a lowest frequency cut-off; see discussions later). Here we point out that the above discussion is based on the linear approximation. In reality, ϕ_1 and ϕ_2 are the coupled fields whose dynamics is modulated by the effective potential. This couples various momentum-modes of the field non-linearly, and makes resonance conditions much more complicated.

The above analysis shows that the higher momentum-modes of fields ϕ_1 and ϕ_2 , following their respective resonance conditions, grow with time. Now, we show how zero-mode of these fields vary with time. The zero-modes of fields characterise the field configuration at each time and provide the frequency of oscillations during the large amplitude oscillation stage of the field. Fig.6 shows the time evolution of real part of zero-modes ($k_x=0$, $k_y=0$) of fields ϕ_1 and ϕ_2 for two sets of parameters of the effective potential. Note that imaginary part of zero-modes for both the fields are zero. In the figure, zero-mode of ϕ_1 field is normalized with the respective Φ_0 value. For this simulation, we have taken $\varepsilon=0.4$ and $\omega=100 \text{ \AA}^{-1}$. Solid(blue) and dash-dotted(gray) plots are the time evolution of zero-modes of fields ϕ_1 and ϕ_2 , respectively, for $\Phi_0=10 \text{ \AA}^{-1}$, $\lambda=40$. In this case, there are oscillations in the ϕ_1 zero-mode during the time interval of 0.5 - 1.5 \AA with growing and then decaying amplitude (we call

it *large amplitude oscillation stage*). From time $t=1.5 \text{ \AA}$ onwards, the oscillations stop and zero-mode starts collapsing towards the zero value. The collapse of zero-mode starts roughly at the time of formation of vortex-antivortex pairs in the system. We have performed the simulations for different spacetime oscillation frequencies and calculated the time evolution of ϕ_1 zero-mode (in the figure, it not shown for other frequencies). We see that in all cases, initially there is a unique frequency and amplitude of oscillations of ϕ_1 zero-mode. Subsequently, this gets modulated with a *new* frequency of oscillations with growing amplitude as shown in Fig.6 from time $t=0.5 \text{ \AA}$. This shows that the very initial time oscillations of ϕ_1 zero-mode (before $t=0.5 \text{ \AA}$ in Fig.6) is independent from the spacetime oscillations, rather, may be related with the evolution of initial field fluctuations. However, the *new* modulation frequency, i.e. the frequency during the time-stage of large amplitude oscillations of ϕ_1 zero-mode, exactly equal to the spacetime oscillation frequency ω (we have shown this later). This gives an another evidence of the *parametric resonance* of the field under the spacetime oscillations.

In Fig.6, ϕ_2 zero-mode, shown by dash-dotted(gray) plot, also has small amplitude oscillations roughly in the same time interval of 0.5 - 1.5 \AA , but without much growth. Later, we have shown that the oscillation frequency of zero-mode of ϕ_2 during this time interval is half of the spacetime oscillation frequency. Here, it should be noted that during this time interval, ϕ_2 varies in between negative and positive values, spatially as well as temporarily, as can be seen from Fig.1(b). Therefore even

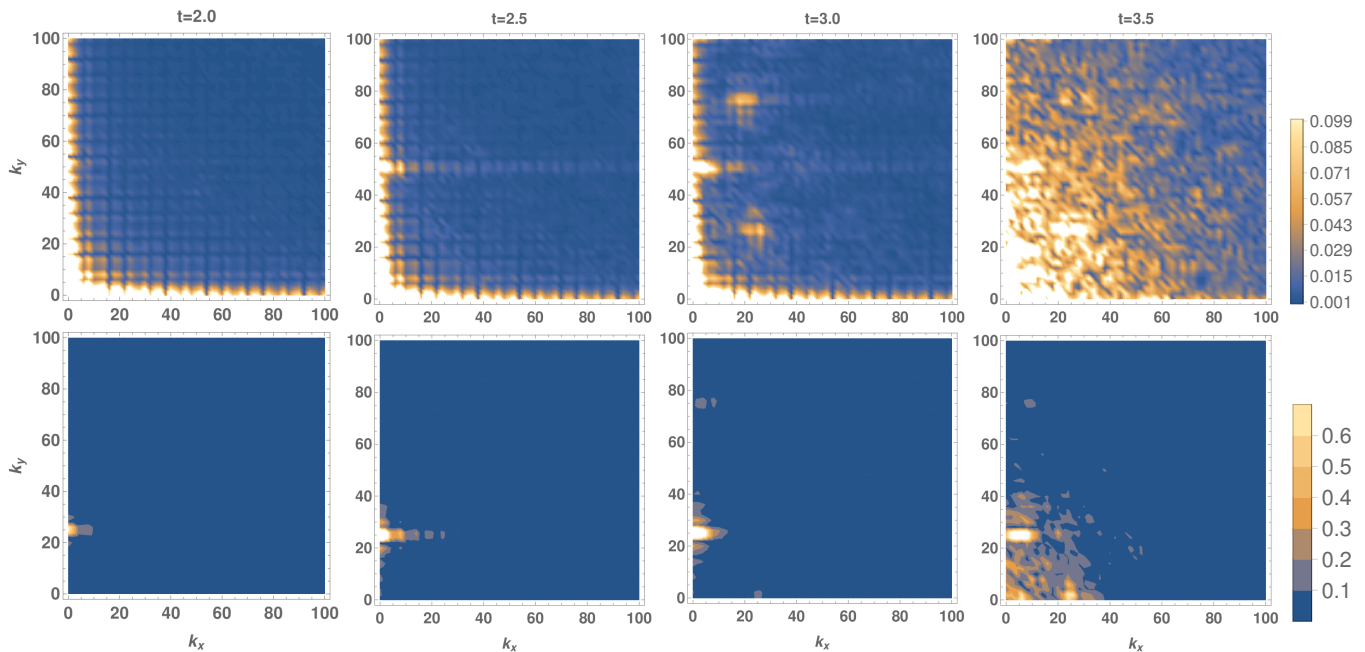


FIG. 5: Figure shows the profile of modulus of field-modes $|\tilde{\phi}_1(\vec{k}, t)|$ (upper panel) and $|\tilde{\phi}_2(\vec{k}, t)|$ (lower panel) at different times for $\omega=50 \text{ \AA}^{-1}$, $\varepsilon=0.4$, $\Phi_0=10 \text{ \AA}^{-1}$, $\lambda=40$. From left to right, modes are plotted at time $t=2.0, 2.5, 3.0, 3.5 \text{ \AA}$. There are noticeable growth of $|\tilde{\phi}_1(\vec{k}, t)|$ at $k_x=0, k_y=\omega$, and growth of $|\tilde{\phi}_2(\vec{k}, t)|$ at $k_x=0, k_y=\omega/2$. In the intermediate stage of field evolution, there are also growth of $|\tilde{\phi}_1(\vec{k}, t)|$ at $k_x \approx \omega/2, k_y \approx \omega/2$ and $k_x \approx \omega/2, k_y \approx 3\omega/2$. The subsequent evolution also leads to the growth of various other momentum-modes of both the fields.

though the absolute value of ϕ_2 reaches a non-zero value in some region, its zero-mode comes out to be very small (just because of the cancellation of positive and negative values). It is already clear from Fig.3, that during this time interval, the growth in the fluctuations of field ϕ_2 is larger in comparison with fluctuations in ϕ_1 . Indeed, the higher momentum-modes of ϕ_2 get growth with time, which we have already seen in Fig.4 at $k_x=\omega/2, k_y=0$ and $k_x=0, k_y=\omega/2$. To show this growth in more detail, in Fig.7, we have plotted the time evolution of real and imaginary part of $(k_x=\omega/2, k_y=0)$ -mode of ϕ_2 with solid(red) and dotted(blue) lines, respectively. This clearly shows oscillations of these modes with growing and then decaying amplitude.

To show the dependence of the zero-modes of fields ϕ_1 and ϕ_2 on the parameters of effective potential, in Fig.6 we have also plotted their time evolution for $\Phi_0=0.1 \text{ \AA}^{-1}$ and $\lambda=4$ with dashed(black) and dotted(red) lines, respectively. In this case, depth of the effective potential is very small, therefore the field can easily overcome the central barrier at $\Phi=0$. Note that in this case, the amplitude of ϕ_1 zero-mode oscillations is small, which is not clearly visible because of the large y -range in the plot. The oscillations in ϕ_2 zero-mode don't have a significant amplitude because of the reason mentioned above.

In order to determine the oscillation frequency of fields during the time interval, say t_i and t_f , in which ϕ_1 zero-mode oscillates with a significantly large amplitude, we

perform Fourier transform of fields' zero-mode from t -space to the frequency f -space,

$$\Pi_i(\vec{k}, f) = \frac{1}{(t_f - t_i)} \int_{t_i}^{t_f} dt \tilde{\phi}_i(\vec{k}, t) e^{-ift}; \quad i = 1, 2. \quad (9)$$

We calculate the *modulus* of $\Pi_1(\vec{k}, f)$ and $\Pi_2(\vec{k}, f)$ fields, which provide the frequency spectrum of momentum-modes of ϕ_1 and ϕ_2 . Fig.8 shows the frequency spectrum of zero-mode of field ϕ_1 during the mentioned time interval for different spacetime oscillation frequencies ω . In the figure, the time interval $t_i - t_f$ for each frequency ω has been mentioned in brackets. To obtain this frequency spectrum, in each case we have subtracted Φ_0 from the zero-mode of ϕ_1 so that the background frequency modes, arise due to constant Φ_0 value, get eliminated and the peak structures become apparent. (However, this subtraction doesn't remove background frequency modes completely, that is the reason a peak at the zero frequency is still present in each plot). In the figure, violet(dotted), green(solid thin), and black(solid thick) lines corresponds to the frequency spectrum for 20, 50, and 100 \AA^{-1} frequencies of spacetime oscillations, respectively. Note that in each case, $\varepsilon=0.4$, $\Phi_0=10 \text{ \AA}^{-1}$, and $\lambda=40$, as taken earlier. It is very clear from the figure, that in each case frequency spectrum has a peak at their respective frequency ω of spacetime oscillations, suggesting the *parametric resonance* of the field. Note that, for the frequency $\omega=50 \text{ \AA}^{-1}$, there are two peaks

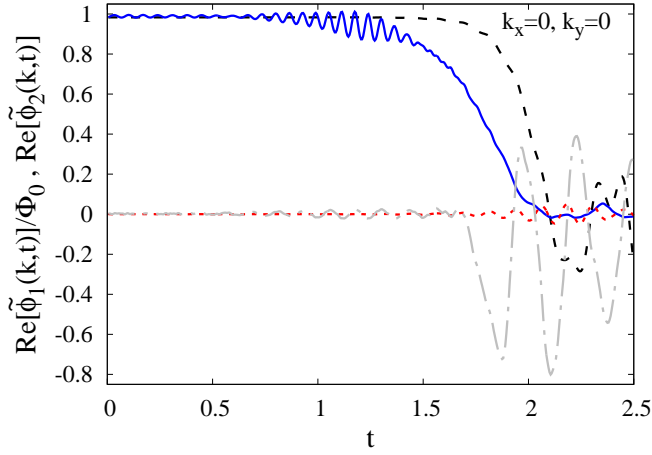


FIG. 6: Figure shows the time evolution of real part of zero-modes of fields ϕ_1 and ϕ_2 for two sets of parameters of effective potential. In the figure, zero-mode of ϕ_1 field is normalized with the respective Φ_0 value. We have taken $\varepsilon=0.4$ and $\omega=100 \Lambda^{-1}$ for the simulation. Solid(blue) and dash-dotted(gray) plots are the time evolution of zero-modes of fields ϕ_1 and ϕ_2 for $\Phi_0=10 \Lambda^{-1}$ and $\lambda=40$, while dashed(black) and dotted(red) plots are for $\Phi_0=0.1 \Lambda^{-1}$ and $\lambda=4$, respectively. Note that there are small amplitude oscillations in dashed(black) plot, which doesn't appear because of large y -range.

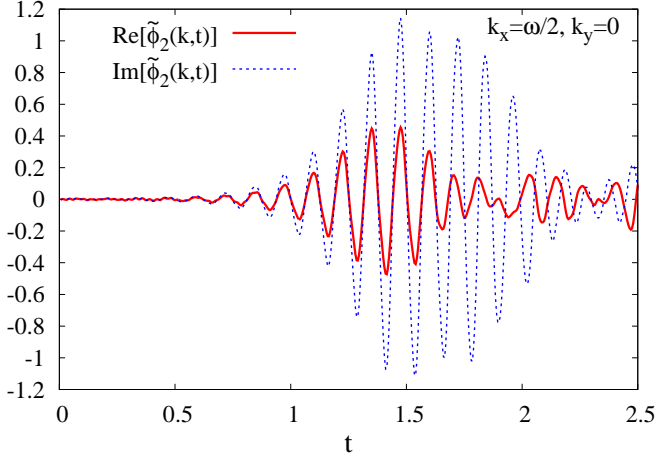


FIG. 7: Figure shows the time evolution of real and imaginary part of $(k_x=\omega/2, k_y=0)$ -mode of field ϕ_2 with solid(red) and dotted(blue) lines, respectively, for $\omega=100 \Lambda^{-1}$, $\varepsilon=0.4$, $\Phi_0=10 \Lambda^{-1}$, $\lambda=40$.

at $f=50 \Lambda^{-1}$ (dominant peak) and at $f=100 \Lambda^{-1}$ (sub-dominant peak) frequencies. The second peak is arising may be due to the coefficient $\sin(2\omega t)$ of the first time derivative term in Eq.(6), or may be due to resonance process itself. For $\Phi_0=0.1 \Lambda^{-1}$ and $\lambda=4$, the amplitude of oscillations of ϕ_1 zero-mode is too small to determine such peak structure, therefore we haven't shown the frequency spectrum for it.

Fig.9 shows the frequency spectrum of zero-mode of field ϕ_2 in the same time interval as mentioned in Fig.8

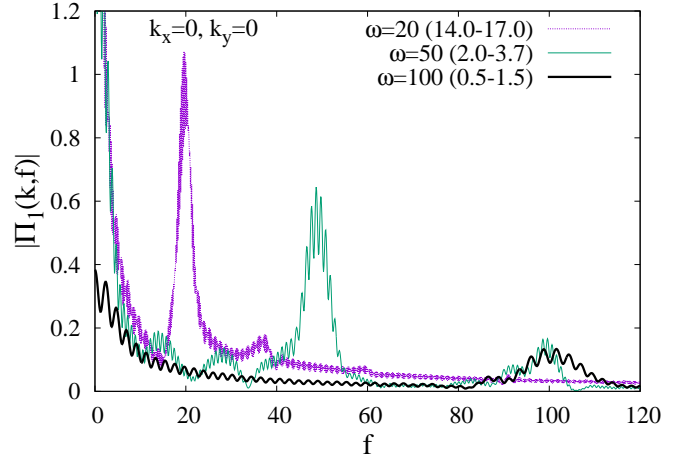


FIG. 8: Figure shows the frequency spectrum of ϕ_1 zero-mode for different spacetime oscillation frequencies ω in the time interval in which it oscillates with a significant large amplitude. This time interval for the respective frequencies has been written in brackets. Violet(dotted), green(solid thin), and black(solid thick) plots correspond to the frequency spectrum for 20, 50, and 100 Λ^{-1} frequencies of spacetime oscillations, respectively. It is very clear in each case, that frequency spectrum has a peak at the corresponding frequency ω of spacetime oscillations, which indicates the phenomena of *parametric resonance* of the field.

for different spacetime oscillation frequencies ω (the time interval $t_i - t_f$ for each frequency ω has been mentioned in brackets). Unlike Fig.8, in this case, there is no background frequency spectrum. In figure, violet(dotted), green(solid thin), and black(solid thick) lines correspond to the frequency spectrum for 20, 50, and 100 Λ^{-1} frequencies of spacetime oscillations, respectively. In this case, each frequency spectrum peaks at half of the spacetime oscillation frequency ω . For $\omega=20 \Lambda^{-1}$, there is no unique and strong peak structure in the frequency spectrum. We have also checked that the real and imaginary part of higher momentum-modes of ϕ_2 (e.g. field-modes at $k_x=\omega/2, k_y=0$ and $k_x=0, k_y=\omega/2$; see Fig.7) also oscillates with the frequency $\omega/2$. In Fig.9, red(dashed) line corresponds to the case for which $\omega=100 \Lambda^{-1}$, $\Phi_0=0.1 \Lambda^{-1}$, and $\lambda=4.0$. In this case also, frequency spectrum peaks at the half of ω , shows the independence from the parameters of the effective potential.

With all these results, it is clear that under the spacetime oscillations, the field Φ itself starts performing oscillations, in space and time, with certain momentum and frequency, by following the resonance condition for a given ω , where ϕ_1 field oscillates with frequency ω , while ϕ_2 goes with frequency $\omega/2$. This shows that the field Φ undergoes *parametric resonance* under the spacetime oscillations.

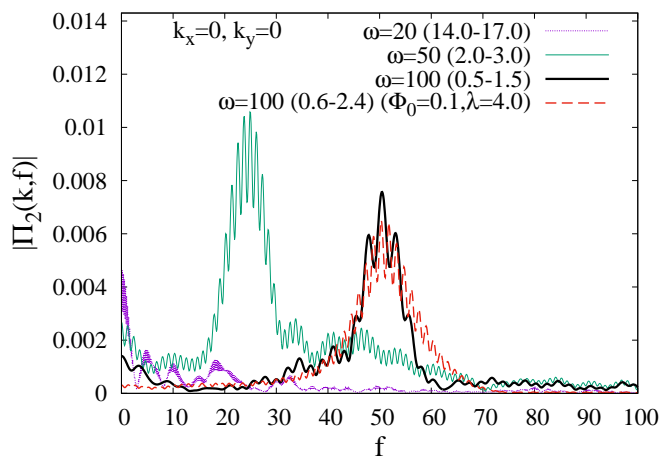


FIG. 9: Figure shows frequency spectrum of ϕ_2 zero-mode for different spacetime oscillation frequencies ω in the time interval as mentioned in Fig.8 (in brackets, mentioned here as well). Violet(dotted), green(solid thin), and black(solid thick) plots correspond to the frequency spectrum for 20, 50, and 100 Λ^{-1} frequencies of spacetime oscillations, respectively. The peak structures show that the zero-mode of ϕ_2 oscillates with $\omega/2$. Red(dashed) plot corresponds to the case, $\omega=100 \Lambda^{-1}$, $\Phi_0=0.1 \Lambda^{-1}$, and $\lambda=4$, which also peaks at $\omega/2$.

B. Frequency dependence of generation of field excitations

As we have discussed earlier, to generate longitudinal excitation dominantly, the frequency of spacetime oscillations should be $\omega > m_\Phi$. In contrary to this, to generate transverse excitation of the field, there is no such frequency cut-off as the mass of modes corresponding to this excitation is zero. Therefore even in the low frequency regime, i.e. $\omega < m_\Phi$, spacetime oscillations can lead to the generation of transverse excitation via the parametric resonance. Thus, there is a fundamental difference in the evolution of field in the frequency regimes $\omega > m_\Phi$ and $\omega < m_\Phi$, and in both the regimes, in principle, the field excitations can be generated under the spacetime oscillations.

In our simulation, we have studied the generation of field excitations and the formation of vortex-antivortex pairs in a wide range of frequencies of spacetime oscillations. At low frequencies, vortex-antivortex pairs form with relatively smaller vortex densities and remain well separated. In this regime, unlike the case of high frequency, field remains close to the VEV of effective potential for a significant time of evolution. This has been depicted in Fig.10, where left panel shows the vector plot of field configuration in the physical space and right panel shows the field distribution in the field-space; both are at time $t=18.5 \Lambda$. For this simulation, the spacetime oscillation frequency is taken $\omega=20 \Lambda^{-1}$, and other parameters of simulation are $\varepsilon=0.4$, $\Phi_0=10 \Lambda^{-1}$, $\lambda=40$ (same as used previously). Left plot clearly shows the formation

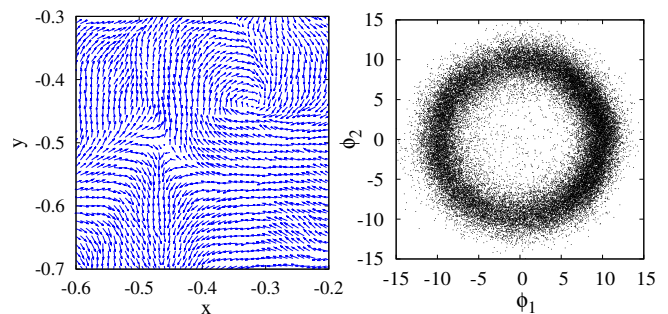


FIG. 10: Figure shows the field configuration in physical space (left panel) and in field-space (right panel) at time $t=18.5 \Lambda$ for the frequency $\omega=20 \Lambda^{-1}$ ($\varepsilon=0.4$, $\Phi_0=10 \Lambda^{-1}$, and $\lambda=40$). Left plot shows the formation of well separated vortex-antivortex pair in the system. Right plot shows that at this frequency of spacetime oscillations, mainly transverse excitation of the field has been generated.

of well separated vortex-antivortex pair in the system. Right plot shows that in almost all lattice points, the field is close to VEV of the effective potential, and the field distribution covers the whole vacuum manifold (starting from a localized distribution). It shows that mainly transverse excitation has been generated in the system, while longitudinal excitation is strongly suppressed in this frequency regime; compare with Fig.2(d).

We mention that in the low frequency regime ($\omega \lesssim 4\pi(\text{system size})^{-1}$; see below), finite size of the system affects the generation of field excitations. This happens because the spacetime oscillations couple to k -modes of the field, where for ϕ_2 field, ($k_{x(y)}=\omega/2$, $k_{y(x)}=0$)-modes dominantly grow with time; see Fig.4 and Fig.5. For finite lattices, the lowest non-zero k -mode which can be present in each direction is $k_L=2\pi/L$, where L is the lattice size. Therefore any frequency ω below the cut-off $2k_L$ cannot generate resonant oscillations of the field; excitations with wavelength larger than the lattice size can not be accommodated. Therefore to excite the field, the frequency of spacetime oscillations should be $\omega \geq 4\pi/L$ or equivalently $f_a \geq 2/L$, where $f_a=\omega/2\pi$. In our simulations, even with frequencies two or three times larger than this cut-off, the field finds difficulties to achieve excitations. We have checked, that increasing lattice size leads to the generation of excitations with a spacetime oscillation frequency at which excitations can not be generated on smaller lattices. This suggests that in principle, any low frequency of spacetime oscillations can excite the field leading to the formation of vortices if a suitable system size is chosen and evolved for a significantly large time; see details in next subsection.

C. The time dependence of formation of vortices on frequency and amplitude of spacetime oscillations

In this section, we present our study on the dependence of the parameters of spacetime oscillations in the formation of vortices. For this, we note down the time t_{vortex} at which the first vortex-antivortex pair forms in the system. We call this time as the *vortex formation time*. To locate the vortices, we compute the variation of phase of Φ around each elementary square of lattice. The variation of phase between any two adjacent points on the elementary square is determined by the *geodesic rule* [24]. By continuity, the phase of a complex scalar field along a loop is always $2\pi n$, where n is an integer. Throughout the evolution of field, we observe only $n=0, \pm 1$ for the variation of phase around each elementary square. We identify the vortex with $n=+1$ and antivortex with $n=-1$. We have checked that t_{vortex} doesn't much depend on the amplitude of fluctuations in the initial field configuration, i.e. on β .

In Fig.11, we have plotted $t_{vortex} \omega/2\pi$ versus ω for $\varepsilon=0.4$. The parameters of the effective potential are $\Phi_0=10 \text{ \AA}^{-1}$ and $\lambda=40$. Note that $t_{vortex} \omega/2\pi$ is a dimensionless number which is equal to the *number of cycle* of spacetime oscillations up to the time t_{vortex} . Figure clearly shows that in the frequency regime $\omega \gtrsim 50 \text{ \AA}^{-1}$, the *number of cycle* required to form vortices is almost independent from ω . However, by lowering the frequency of spacetime oscillations below 50 \AA^{-1} , this number starts increasing. We haven't seen the formation of any vortices below $\omega=16 \text{ \AA}^{-1}$ up to a significantly large time on the used lattice.

We have already mentioned, that in the low frequency regime, finite size of the system plays an important role in the generation of field excitations and therefore formation of vortices as well. For example, in our simulation, up to a significantly large time, there is no formation of any vortex-antivortex pair on 200×200 lattice at frequency $\omega=15 \text{ \AA}^{-1}$, however with the same parameters of simulation, vortices form on 800×800 lattice. Therefore, it may be possible that in Fig.11, the deviation of $t_{vortex} \omega/2\pi$ below $\omega=50 \text{ \AA}^{-1}$ from a constant value arises due to the finite size effects of the system. Therefore, it may also be possible that this constant value of $t_{vortex} \omega/2\pi$ is a universal number for the formation of vortices and may remain true even in the low frequency regime when the finite size effects get eliminated.

To investigate it in more detail, we have performed simulations at different system size L , frequencies ω , and boundary conditions. As we have mentioned earlier, in our simulations, we have used periodic boundary conditions (PBCs). These boundary conditions affect our simulation results very strongly in the regime where finite size effects dominate. In general, we observe finite size effects in our simulation when frequency ω becomes $\lesssim 4\pi/L$ or equivalently when $L\omega/4\pi \lesssim 1$. To show these

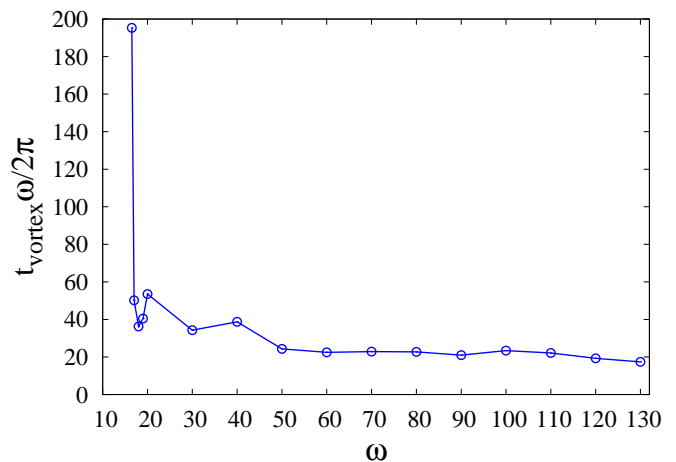


FIG. 11: Figure shows the dependence of vortex formation time t_{vortex} on various frequencies ω . In figure, we have plotted the *number of cycle* of spacetime oscillations up to the time t_{vortex} , i.e. $t_{vortex} \omega/2\pi$, versus ω . For this plot, parameters are, $\varepsilon=0.4$, $\Phi_0=10 \text{ \AA}^{-1}$, and $\lambda=40$. Figure clearly shows that in the frequency regime $\omega \gtrsim 50 \text{ \AA}^{-1}$, $t_{vortex} \omega/2\pi$ is almost independent from ω . However, by decreasing the frequency ω below 50 \AA^{-1} , this number starts increasing.

effects explicitly, and effects of boundary conditions in general, we have studied effects of changing lattice size L on t_{vortex} by keeping ω and ε fix. We have also studied the effects of using different boundary conditions on t_{vortex} . We show below that t_{vortex} for simulations using fix boundary conditions (FBCs) are relatively lesser affected with finite size effects in comparison with simulations using PBCs. In Fig.12, we have plotted $t_{vortex} \omega/2\pi$ versus $L\omega/4\pi$ (both are dimensionless numbers) for two different boundary conditions and at two frequencies ω , $\omega_1=100 \text{ \AA}^{-1}$ and $\omega_2=50 \text{ \AA}^{-1}$, where for each curve ω and $\varepsilon(=0.4)$ are fixed. The parameters of effective potential are $\Phi_0=10 \text{ \AA}^{-1}$ and $\lambda=40$. In this figure, curves blue (circle) and black (square) are for simulations using PBCs at frequencies ω_1 and ω_2 , respectively. While curves red (triangle) and brown (star) are for simulations using FBCs, again, at frequencies ω_1 and ω_2 , respectively. Under the spacetime oscillations, the lowest cut-off for $L\omega/4\pi$ to generate field excitations is 1, which must also be a cut-off for formation of vortices in the system. Therefore when $L\omega/4\pi$ approaches 1 from higher values, one would expect a growth in $t_{vortex} \omega/2\pi$ which must diverge at $L\omega/4\pi \lesssim 1$. This is what we see in the figure, where in each curve, beyond the lowest $L\omega/4\pi$ points, t_{vortex} diverges.

We see that when $L\omega/4\pi$ is sufficiently larger than 1 (say, greater than ~ 10), $t_{vortex} \omega/2\pi$ remains almost invariant with increasing $L\omega/4\pi$, and takes a constant value $\simeq 23$, which seems to be a universal number, independent from choice of boundary conditions and ω . While when $L\omega/4\pi$ starts approaching 1 (say, becomes lesser than ~ 10), $t_{vortex} \omega/2\pi$ starts increasing due to

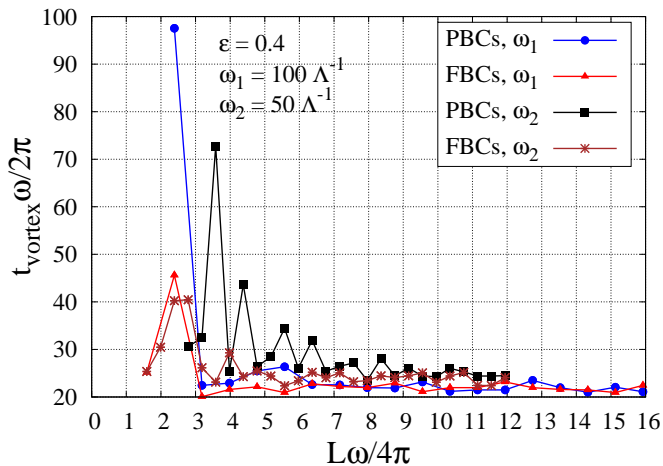


FIG. 12: Figure shows the effects of using different boundary conditions on t_{vortex} at different system size L and at two different ω , $\omega_1=100 \Lambda^{-1}$ and $\omega_2=50 \Lambda^{-1}$, where for each curve ω and ε are fixed. The parameters of effective potential are $\Phi_0=10 \Lambda^{-1}$ and $\lambda=40$. Curves blue (circle) and black (square) are for simulations using periodic boundary conditions (PBCs) at frequencies ω_1 and ω_2 , respectively. While curves red (triangle) and brown (star) are for simulations using fix boundary conditions (FBCs), again, at frequencies ω_1 and ω_2 , respectively. In each curve, beyond the lowest $L\omega/4\pi$ points, t_{vortex} diverges.

finite size effects and diverges when $L\omega/4\pi$ reaches very close to 1 (say, $\simeq 2$ for PBCs, and $\simeq 1.5$ for FBCs). We have seen that in the case of FBCs, the deviation in $t_{vortex} \omega/2\pi$ from such universal value is lesser in comparison with PBCs. Also, there are small lattice sizes in which when we use PBCs, vortices don't form, while when we use FBCs, vortices form. Thus with FBCs, vortices could be formed easily in comparison with PBCs. It must be appreciated, that for both boundary conditions, the number of cycle of spacetime oscillations to form first vortex-antivortex pair in the system are roughly same at $L\omega/4\pi \gg 1$ and independent from frequency ω . Thus, this study is clearly indicating that there is a universal number of cycle of spacetime oscillations to form first vortex-antivortex pair in the system if there are no finite size effects. All in all, our investigation suggests that even with a small frequency ω , field may get excited (transverse excitation) under the spacetime oscillations if one performs simulation on a sufficiently large lattice ($L \gg 4\pi/\omega$) and evolves for a significantly long time ($t \gtrsim t_{vortex} \simeq 46\pi/\omega \simeq \frac{3}{2} \frac{\pi^4}{\omega}$).

In Fig.13, we have presented the effect of ε on t_{vortex} . For this plot, we have taken $\omega=100 \Lambda^{-1}$, $\Phi_0=10 \Lambda^{-1}$, and $\lambda=40$. Figure clearly shows that decreasing ε causes more time to form vortex-antivortex pair in the system. For lower values of ε , system takes longer time to achieve field excitations, and the large amplitude field oscillation stage persists for a longer time. In the regime of very small ε , the field excitations don't grow sufficiently to

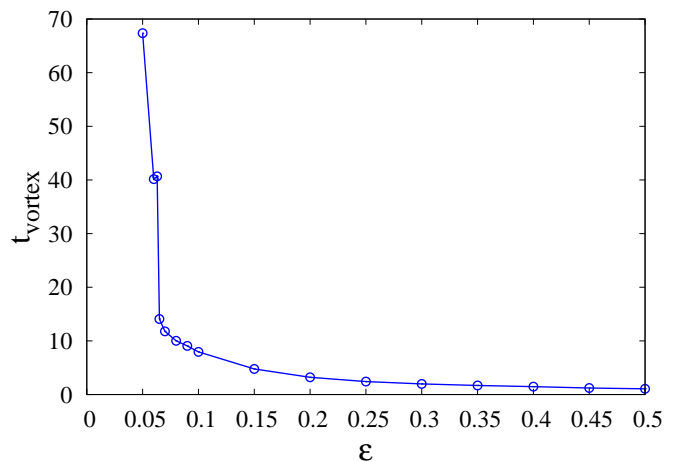


FIG. 13: Figure shows the effect of ε on t_{vortex} . For this plot, we have taken $\omega=100 \Lambda^{-1}$, $\Phi_0=10 \Lambda^{-1}$, and $\lambda=40$.

create vortices in the system. This behavior of field response to ε is also a feature of *parametric resonance*, in which the resonant growth is strongly suppressed by decreasing the magnitude of time dependent parameter(s) of the oscillator [23].

D. Formation of vortex-antivortex lattice under spacetime oscillations

The formation of vortex-antivortex lattice structure has interest in various condensed matter systems. In refs.[25–27], the formation of such lattices has been studied in superconducting films with magnetic pinning arrays, ultra-cold fermionic gases in two-dimensions, and superconducting twisted-bilayer graphene. The melting of vortex-antivortex lattice in two-dimensional Fermi gases has been studied in ref.[28]. For certain parameters of the simulation, we have also seen the formation of vortex-antivortex lattice structure under the spacetime oscillations. In Fig.14, we have shown the phase (left panel) and magnitude (right panel) of the field Φ at two different times of field evolution. The parameters of the simulation are $\omega=17 \Lambda^{-1}$, $\varepsilon=0.4$, $\Phi_0=0.1 \Lambda^{-1}$, and $\lambda=4$. We have mentioned previously, that when $\omega \gg m_\Phi$, the formed vortices under the spacetime oscillations are not topological in nature. For the above parameters of the simulation also $\omega \gg m_\Phi$, therefore the formed vortices, which we see in Fig.14, don't satisfy the properties of topological vortices. One can clearly see that the core size of these vortices is much lesser than m_Φ^{-1} , indeed it is given by $\sim \omega^{-1}$, and the field values outside these vortices reach up to six times of VEV. Fig.14(1a) and Fig.14(1b) show the phase and magnitude of the field Φ at time $t=28.65 \Lambda$, while Fig.14(2a) and Fig.14(2b) show the same at time $t=29.4 \Lambda$. On the plots, circles and triangles indicate the location of vortices and antivortices,

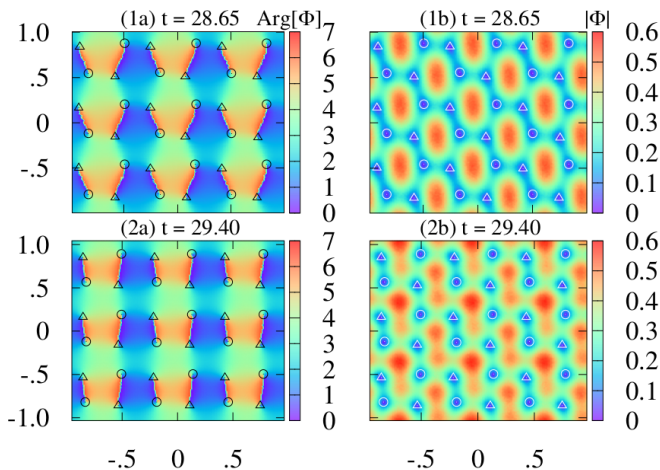


FIG. 14: Figure shows the formation of vortex-antivortex lattice structure in the system. The parameters of the simulation are $\omega=17 \Lambda^{-1}$, $\varepsilon=0.4$, $\Phi_0=0.1 \Lambda^{-1}$, and $\lambda=4$. Plots (1a) and (1b) show the phase and magnitude of field Φ at time 28.65Λ , while plots (2a) and (2b) show the same at time 29.4Λ . With the distribution of phase and magnitude of field, one can notice a structure of vortex-antivortex lattice, which has been depicted by pointing the locations of vortex and antivortex with circles and triangles, respectively.

respectively. Correspondingly, in the left panel, there is a variation of $\pm 2\pi$ in the phase of Φ at the location of these points. The $\pm 2\pi$ phase variations correspond to the vortex and antivortex configurations, respectively. In the right panel, these points correspond to the places where the magnitude of Φ is zero. One can clearly notice that there is a vortex-antivortex lattice structure in both, upper and lower, panels. We have seen, that this lattice structure keeps on changing with time. We have checked that the formation of this structure has nothing to do with the amplitude of initial fluctuations, i.e. on the value of β . It may be possible that such lattice structure is arising because of using the periodic boundary condition in the simulation.

V. CONCLUSION AND FUTURE OUTLOOK

In this work, we have performed (2+1)-dimensional simulations for a complex scalar field in the presence of oscillating spacetime metric background. We have considered spacetime metric as a time-dependent periodic perturbation on the top of the Minkowski metric. The field is taken on the VEV of U(1) symmetry breaking effective potential, and small spatial fluctuations in the initial field configuration has been considered. We see that depending upon the amplitude and frequency of the metric, field undergoes *parametric resonance*, which causes the generation of field excitations and leads to the formation of vortex-antivortex pairs in the system. We find that there is a fundamental difference in the evolution of

field in the frequency regimes $\omega > m_\Phi$ and $\omega \leq m_\Phi$. In the low frequency regime mainly transverse excitation arises, and well separated vortex-antivortex pairs form in the system. While in the high frequency regime, longitudinal excitation of the field also gets generated dominantly.

In our simulation, finite size effects restrict the generation of field excitations in the regime where $L\omega/4\pi \lesssim 1$, where L is the system size, and ω is the frequency of spacetime oscillations. Our study suggests that in principle any low frequency can excite the field if suitable system size is chosen ($L \gg 4\pi/\omega$), and the field is evolved for a significantly long time ($t \gtrsim \frac{3}{2} \frac{\pi^4}{\omega}$). We have studied the effects of frequency, boundary conditions, and system size on the *number of cycle* of spacetime oscillations required to form first vortex-antivortex pair in the system. Our study suggests that there is a universal number of cycle of spacetime oscillations to form first vortex-antivortex pair in the system if there are no finite size effects. The formation of vortices also depends on the amplitude of spacetime oscillations; the vortex formation time increases by decreasing amplitude. For certain parameters of the simulation, we have also seen the formation of vortex-antivortex lattice structure, however, these vortices are not topological vortices as in such case $\omega \gg m_\Phi$ (m_Φ is the field-mass) for which there is no possibility of formation of topological vortices. Only in the case of $\omega \lesssim m_\Phi$, the formed vortices under the spacetime oscillations are topological in nature.

Throughout this work, we have completely ignored the back reaction of energy density perturbations of the field on the spacetime metric. As we see the formation of vortices in our simulation, and a vortex configuration carries an energy density profile with maximum value in the vortex core. Therefore depending upon the energy of the configuration, it can cause changes in the spacetime manifold, which can affect the further evolution of the field. It will be interesting to see how the field evolves under such a complete scenario. We will try to pursue this in our future work.

To study the time evolution of the condensate field of neutron stars superfluidity during the BNS merger, a full (3+1)-dimensional simulation with an appropriate time dependent deformation of star metric is required. It will reveal whether the time scale and length scale of the whole process are sufficient to excite the condensate field to lead the formation of vortex-antivortex pairs in the interior superfluid. Our present study suggests that there is no possibility of having condensate excitations of neutron star superfluidity under the phenomena of parametric resonance due to finite size effects. However, a detailed investigation is needed to determine if there is any other possibility of the generation of condensate excitations. This, we will try to pursue in future.

The present work has its applications in other systems also. For example, the *second homotopy group* of S^2 -manifold is non-trivial, i.e. $\pi_2(S^2) = \mathbb{Z}$ [3], therefore

this manifold allows the existence of *topological texture* in (2+1)-dimensions (baby Skyrmion) and *topological monopole* in (3+1)-dimensions. Similarly, S^3 -manifold (group space of $SU(2)$) allows the existence of *topological texture* in (3+1)-dimensions as the *third homotopy group* $\pi_3(S^3)=\mathcal{Z}$ [3]. These topological objects have their cosmological interests, formation of which can also be studied under the spacetime oscillations (similar to the formation of vortices presented in this paper). In the *abelian-Higgs model* and pure $U(1)$ gauge theory also, one can study the formation of flux-tubes and generation of magnetic field, respectively, under these oscillations.

This study can also be extended for the $U(1)$ -symmetry broken effective potential with a small explicit symmetry breaking term. In such case, there must be a lowest frequency cut-off of spacetime oscillations for the generation of field excitations set by the mass of pseudo-Goldstone modes; only frequencies higher than or equal to the mass of these modes can lead the field excitations. In our simulation, we have seen the field excitations in the presence of such term (we haven't presented this here). This result can be utilized in the generation of excitations of the *axion-like* field carrying mass $\sim 10^{-22} - 10^{-21}$ eV [29] and coupled with the spacetime oscillations. The *axion-like* particles having above mass range are considered to be a possible dark matter candidate, known as the 'wave dark matter' or 'fuzzy dark matter' (FDM) [29]. To excite this field, correspondingly, the frequency of spacetime oscillations should be $\gtrsim 0.1 - 1$ μHz . This can be easily achieved by the BNS [15] and black-hole merger [30] systems, which produce gravitational waves (GW) in the frequency range of $\sim 10\text{Hz} - 1\text{kHz}$ with a significantly large strain amplitude. We expect that a sustained spacetime oscillation will give rise excitation of *axion-like* field over a length scale having momentum of field corresponding to the frequency of spacetime oscillations. The effect will be more pronounced in the nearest region of GW source as the strain amplitude is significantly large there. If such excitation arise, then as soon as GWs completely pass away, the field will start rolling towards the minima of effective potential and perform coherent oscillations at various constant- r hypersurfaces about the source. We will present this phenomena in detail in our future work.

ACKNOWLEDGEMENTS

We are very grateful to Ajit M. Srivastava and Subhrooneel Chakrabarti for very useful discussions, suggestions, and comments on the manuscript. We also would like to thank A.P. Balachandran, P.S. Saumia, Abhishek Atreya, T.P. Sreeraj, Nirupam Dutta, and Minati Biswal for useful discussions and comments on the work.

[†] Electronic address: digal@imsc.res.in

- [1] W.H. Zurek, Phys. Rep. **276**, 177 (1996).
- [2] A. Rajantie, Int. J. Mod. Phys. **A17**, 1 (2002).
- [3] N.D. Mermin, Rev. Mod. Phys. **51**, 591 (1979).
- [4] T.W.B. Kibble, J. Phys. **A9**, 1387 (1976); Phys. Rept. **67**, 183 (1980).
- [5] L.D. Landau and E.F. Lifshitz, **Statistical Physics Part 2**, Pergamon Press Ltd. (1980).
- [6] D.R. Tilley and J. Tilley, **Superfluidity and Superconductivity**, Third Edition, Overseas Press (2005).
- [7] S. Digal, R. Ray, S. Sengupta, and A.M. Srivastava, Phys. Rev. Lett. **84**, 826 (2000).
- [8] R. Ray and S. Sengupta, Phys. Rev. D **65**, 063521 (2002).
- [9] E.A.L. Henn, J.A. Seman, G. Roati, K.M.F. Magalhães, and V.S. Bagnato, Phys. Rev. Lett. **103**, 045301 (2009); E.A.L. Henn et al., Phys. Rev. A **79**, 043618 (2009).
- [10] V.I. Yukalov, A.N. Novikov, V.S. Bagnato, Phys. Lett. A **379**, 1366 (2015).
- [11] V.I. Yukalov, E.P. Yukalova, and V.S. Bagnato, Phys. Rev. A **66**, 043602 (2002).
- [12] R.E. Packard, Phys. Rev. Lett. **28**, 1080 (1972).
- [13] D.G. Yakovlev, A.D. Kaminker, and K.P. Levenfish, Astron. Astrophys. **343**, 650 (1999).
- [14] M.G. Alford, A. Schmitt, K. Rajagopal, and T. Schäfer, Rev. Mod. Phys. **80**, 1455 (2008).
- [15] B.P. Abbott et al. (LIGO Scientific Collaboration and Virgo Collaboration), Phys. Rev. Lett. **119**, 161101 (2017).
- [16] **Gribov-80 Memorial Volume; Quantum Chromodynamics And Beyond**, C.N. Colacino, page 449-454, World Scientific (2010).
- [17] A. Perego, S. Bernuzzi, and D. Radice, Eur. Phys. J. A **55**:124 (2019).
- [18] L. Amundsen and E. Ostgaard, Nucl. Phys. **A 437**, 487 (1985); Nucl. Phys. **A 442**, 163 (1985).
- [19] J. Anandan, Phys. Rev. Lett. **47**, 463 (1981).
- [20] A. Schmitt, **Introduction to Superfluidity; Field-theoretical Approach and Applications**, Springer (2015).
- [21] C. Xiong, M.R.R. Good, Y. Guo, X. Liu, and K. Huang, Phys. Rev. D **90**, 125019 (2014).
- [22] S. Carroll, **Spacetime and Geometry; An Introduction to General Relativity**, Addison Wesley (2004).
- [23] L.D. Landau and E.F. Lifshitz, **Mechanics; Third Edition**, Elsevier (2007).
- [24] M.J. Bowick, L. Chandar, E.A. Schiff, and A.M. Srivastava, Science **263**, 943 (1994); [hep-ph/9208233].
- [25] M.V. Milošević and F.M. Peeters, J. Low Temp. Phys. **139**, 257 (2005).
- [26] S.S. Botelho and C.A.R. Sá de Melo, Phys. Rev. Lett. **96**, 040404 (2006).
- [27] Y. Su and S.-Z. Lin, Phys. Rev. B **98**, 195101 (2018).
- [28] G. Cao, L. He, and X.-G. Huang, Phys. Rev. A **96**, 063618 (2017).
- [29] L. Hui, J.P. Ostriker, S. Tremaine, and E. Witten, Phys. Rev. D **95**, 043541 (2017).
- [30] B.P. Abbott et al. (LIGO Scientific Collaboration and Virgo Collaboration), Phys. Rev. Lett. **116**, 061102 (2016).

* Electronic address: shreyanshsd@imsc.res.in